

## Fenton-like reaction and photocatalysis using ferrous oxalate and g-C<sub>3</sub>N<sub>4</sub> enhancing reactive oxygen species for dye wastewater degradation under visible-light irradiation

Shaomin Liu<sup>a,b,\*</sup>, Xiaoxiao Wang<sup>b</sup>, Jianshu Zhang<sup>b</sup>

<sup>a</sup>Key Laboratory of Safe and Effective Coal Mining (Anhui University of Science and Technology), Ministry of Education, Huainan 232001, China, Tel. +86 554 6668742; email: shmliu1@163.com (S. Liu)

<sup>b</sup>School of Earth Science and Environmental Engineering, Anhui University of Science and Technology, Huainan 232001, China, Tel. +15697560245; email: 1754215288@qq.com (X. Wang), Tel. +15855452975; email: 11710659997@qq.com (J. Zhang)

Received 17 September 2019; Accepted 7 March 2020

### ABSTRACT

In this study, a catalyst material consisting of g-C<sub>3</sub>N<sub>4</sub> and ferrous oxalate was synthesized via a simple and environment-friendly method. Then, the catalyst was characterized using various techniques. The photocatalytic performance of the catalysts in the degradation of Rhodamine B was evaluated under visible-light irradiation. Based on the experimental results, the combination of g-C<sub>3</sub>N<sub>4</sub> and ferrous oxalate was crucial to enhance the separation of charge carriers and improve the O<sub>2</sub> reduction under visible light. This process also promoted the production of hydroxyl radicals (<sup>•</sup>OH). In the system, oxalate was used to assist the conversion between Fe<sup>2+</sup> and Fe<sup>3+</sup>, with the chelation of Fe<sup>3+</sup> to form a complex, to avoid the formation of sludge. Furthermore, without the addition of hydrogen peroxide (H<sub>2</sub>O<sub>2</sub>), the system had efficient photodegradation with excellent effect. This study provided an innovative idea for the application of ferrous oxalate in photocatalysis and Fenton-like reaction.

*Keywords:* Ferrous oxalate; g-C<sub>3</sub>N<sub>4</sub>; Photocatalytic; Rhodamine B; Characterization

### 1. Introduction

Advanced oxidation technologies, such as photocatalysis [1], electrochemistry [2], and Fenton oxidation [3], have gained widespread attention as efficient and simple methods for wastewater treatment. Among these technologies, photocatalytic technology has shown great advantages in pollutant degradation in recent years. Semiconductor materials produce free radicals under sunlight. These radicals can degrade organics or redox heavy metals in water without any harmful products. Graphitic carbon nitride (g-C<sub>3</sub>N<sub>4</sub>, referred to as CN hereinafter) is a good nonmetallic catalyst and can be excited photons and holes under visible-light irradiation. In addition, CN is extremely stable and easy to

synthesize [4,5]. Despite its unique advantages, carriers can couple quickly and be utilized lowly. Thus, researchers have proposed numerous approaches, such as co-doping [6,7], with other semiconductor to form heterojunctions [8,9], deposition with precious metal [10,11], and controlling the morphology [12], with metal organic framework to form composites [13,14], to enhance the photocatalytic activity of CN.

Homogeneous Fenton oxidation is a simple method in which the generated hydroxyl radicals (<sup>•</sup>OH) can decompose most contaminants. However, the sludge in the reaction produces secondary pollution, and the cycle efficiency of Fe<sup>2+</sup> and Fe<sup>3+</sup> is slightly low. Thus, H<sub>2</sub>O<sub>2</sub> may be not utilized effectively in pollutant degradation. As a result,

\* Corresponding author.

heterogeneous Fenton oxidation technology, which can easily reuse catalysts and avoid the byproducts of sludge, has been rapidly developed in recent years. Ferrous oxalate dihydrate (referred to as FOD hereinafter) is one of the simplest coordination polymers with high catalytic performance and works as an excellent catalyst in heterogeneous Fenton reaction. FOD is relatively stable and easy to reuse because it is usually undissolved or insoluble in most organic solvents or water [15,16]. The block of FOD is composed of a chain-like structure in which the repeated units formed by the coordination of two oxalic acid groups and ferrous metal are in the axial direction; by contrast, the coordination of each ferrous metal with two water molecules is in the longitudinal direction. As a result, FOD has a stable six-coordination structure [17]. The FOD crystal belongs to *n*-type semiconductors and can be divided into  $\alpha$  and  $\beta$  phases. In many experiments, FOD is used as a catalyst to degrade pollutants and can achieve a high catalytic effect with the assistance of other substances. For instance, FOD has been used to activate  $H_2O_2$  in heterogeneous Fenton processes [18,19]. Furthermore, FOD has been used to treat pollutants under visible light with the assistance of an organic reductant (citric acid or oxalic acid) [20,21]. In the above instances, although the wastewater was degraded, the overall process was not economic. This work takes advantage of the effect of visible light on the composite catalyst, mainly using the photoexcitation of CN with visible light to produce  $e^-$  and  $h^+$  in promoting the FOD degradation of contaminants. The combination of FOD and CN is applied in photocatalytic and Fenton-like technology to treat pollutants. The carrier utilization rate is improved, and the reduction capacity of  $O_2$  under visible light is enhanced. Moreover, the preparation of catalyst materials is simple, mild, economical, and environment friendly. Rhodamine B (RhB) is considered harmful to humans and the environment and has a high chroma even at a low concentration of wastewater. Accordingly, RhB is used to estimate the catalytic effect of composite materials.

## 2. Experiment

### 2.1. Reagents and materials

Melamine was purchased from the Tianjin Damao Chemical Reagent Factory.  $FeSO_4 \cdot 2H_2O$  was purchased from Tianjin Kaitong Chemical Reagent Co., Ltd.  $C_2H_2O_4 \cdot 2H_2O$  was purchased from Shanghai Reagent First Factory Comprehensive Operation Company. RhB was purchased from Tianjin Guangfu Fine Chemical Research Institute. Ethyl alcohol, *tert*-butanol, *p*-benzoquinone, and potash iodide were purchased from Sinopharm Chemical Reagent Co., Ltd., (Shanghai, China). The reagents in this study were of analytical grade and used without any purification.

### 2.2. Synthesis of catalysts

CN was prepared using a thermal polycondensation method. First a suitable amount of melamine was placed in a ceramic crucible and placed into the muffle furnace (550°C, 3 h). Then the melamine was naturally cooled to room temperature and ground to obtain yellow CN powders.

Subsequently,  $C_2H_2O_4 \cdot 2H_2O$  and  $FeSO_4 \cdot 2H_2O$  (with a mole ratio of 1.5:1) were added to ethanol and ultrapure water, respectively. Then the latter solution was added to the former drop by drop. The mixture was stirred constantly (40°C, 1 h) and aged for 7 h. The resulted precipitates were collected through centrifugation, washed by ultrapure water and ethanol water, and dried in an air-drying oven (40°C, 48 h) to obtain the FOD powder.

On the basis of the theoretical calculation, the catalyst materials with different FOD amounts (5, 10, 20, 30, and 50 wt.%) were prepared to obtain improved catalysts; the materials were denoted as 5-FOD-CN, 10-FOD-CN, 20-FOD-CN, 30-FOD-CN, and 50-FOD-CN, respectively. The CN and FOD powders were dispersed in 110 mL ultrapure water under constant stirring (50°C, 90 min) to synthesize FOD-CN. Then, the final FOD-CN products were obtained through operations, including precipitation, centrifugation, washing through ultrapure water and ethanol, drying, and grinding.

### 2.3. Characterization

The morphology of the catalysts was observed using a scanning electron microscope (SEM; JSM-7500F, USA). The elements contained in the catalyst and their contents were analyzed using an energy dispersive X-ray (EDX) analyzer, usually combined with SEM. An X-ray diffraction (XRD) analyzer (Bruker D8 X-ray, DE) was used to analyze the phase and chemical composition of the catalysts. The parameters of the Bruker D8 X-ray (DE) are as follows: an X-ray source of  $CuK \alpha$  ray ( $\lambda = 1.54178$  nm), an interval of 0.02, a pipe pressure of 40 kV, a pipe flow of 40 mA, a scanning speed of  $6 \text{ min}^{-1}$ , a  $2\theta$  scanning range of  $5^\circ$ – $90^\circ$ . Fourier transform infrared (FTIR) spectroscopy (Thermo Scientific Nicolet iS50, USA) was used to study the chemical composition of the catalysts with a wavelength range of  $400$ – $4,000 \text{ cm}^{-1}$ . The chemical composition and bond energy of the catalysts were analyzed using an X-ray photoelectron spectrometer (Escalab 250Xi) produced by Thermo Fisher Scientific Company; in which the excitation light source was Al K $\alpha$ . The specific surface areas of the samples were analyzed via the Brunauer–Emmett–Teller method (Micro for TriStar II Plus 2.02). A UV-Vis diffuse reflectance spectrometer was used to measure the absorbance of the catalysts. Photoluminescence (PL) spectra were tested using a fluorescence spectrophotometer (fls980 Edinburgh, UK) to measure the effective charge transfer of the catalysts.

### 2.4. Pollutant degradation experiment

The photocatalytic experiments were conducted in the photocatalytic reactor in which both the catalyst (0.1 g) and the pollutant RhB ( $10 \text{ mg L}^{-1}$  200 mL) were added under visible light source (300 W). The mixture was stirred at a constant rate. First, the mixture was reacted in the dark for 30 min to make the catalyst reach the adsorption saturation, and the reaction was performed under visible light. Every 20 min, 6 mL sample was taken out, centrifuged, and filtered through a  $0.22 \mu\text{m}$  polytetrafluoroethylene filter. Then, the supernatant fluid was obtained and the absorbance was measured using a UV-Vis spectrophotometer at 554 nm.

### 3. Results and discussion

#### 3.1. Characterization of materials

The SEM image and EDX spectrum of CN and 10-FOD-CN are shown in Fig. 1. The pure CN had a typical lamellar structure (Fig. 1a), and the rod-shaped FOD crystal [22] was distinctly deposited on the surface of CN (Fig. 1b). Moreover, the EDX image confirmed that the composites contained C, N, O, and Fe atoms in with proportions of 34.79%, 50.95%, 13.31%, and 0.96%, respectively (Fig. 1c). The proportions of the elements indicated that the FOD content was low in FOD-CN.

The chemical phases and composition of the catalysts were detected via XRD (Fig. 2). In the XRD image of CN, two relatively strong diffraction peaks ( $2\theta$  at  $13.0^\circ$  and  $27.6^\circ$ ), which are well matched with the standard card (ICSD code: 87–1526), were observed. The diffraction peak at  $13.0^\circ$  corresponded to the (100) planes of the ordered repetition of triazine units, and the diffraction peak at  $27.6^\circ$  corresponded to the (002) planes of the interlayer accumulation of the aromatic systems [23]. In the XRD image of FOD, three remarkable peaks, which coincided with the standard card of  $\alpha$ -FOD (ICSD code: 23-0293), were observed ( $2\theta$  at approximately  $18.6^\circ$ ,  $23.0^\circ$ , and  $29.8^\circ$ ). All the characteristic diffraction peaks of FOD and CN appeared in the XRD image of FOD-CN with different content proportions, indicating that the FOD presence did not destroy the CN structure. In addition, with the increase in FOD, the intensity of

the diffraction peak of CN gradually decreases, whereas that of FOD gradually increases.

The chemical composition and structure of CN and FOD-CN were investigated via FTIR spectroscopy, as shown in Fig. 3. Similar characteristic peaks appeared in the CN and FOD-CN spectra. The absorption band at  $3,100$ – $3,350\text{ cm}^{-1}$  was related to the stretching vibration zone of the N–H group [24]. The weak band at  $2,160\text{ cm}^{-1}$  was ascribed to the tensile vibration of  $-\text{C}\equiv\text{N}$  [25]. The absorption band at  $1,200$ – $1,650\text{ cm}^{-1}$  was ascribed to the stretch vibration region of the aromatic ring C=N and the C–N bond [26]. The detected peak at  $807\text{ cm}^{-1}$  was ascribed to the tensile vibration of triazine ring [27]. In the FOD FTIR spectrum, the band at approximately  $3,350\text{ cm}^{-1}$  may be due to O–H tensile vibration. The peaks at  $1,317$  and  $1,362\text{ cm}^{-1}$ ,  $1,628\text{ cm}^{-1}$  may be ascribed to the symmetric and asymmetric tensile vibrations of O–C–O [28]. The band at  $820\text{ cm}^{-1}$  may be ascribed to the bending vibration of C=C–O. The peak at  $494\text{ cm}^{-1}$  was ascribed to the stretch vibration of Fe–O [29]. Unfortunately, the absorption band of FOD was almost not observed in the FT-IR spectrum of FOD-CN, possibly due to the low FOD content. However, with the increase in FOD content, the strength of the vibration zone of FOD-CN slightly changed. In particular, as the FOD content increased, the absorption bands at  $3,350\text{ cm}^{-1}$  and  $1,200$ – $1,650\text{ cm}^{-1}$  evidently enhanced, and the tensile strength at  $494\text{ cm}^{-1}$  was slightly enhanced. These results proved the existence of FOD in FOD-CN.

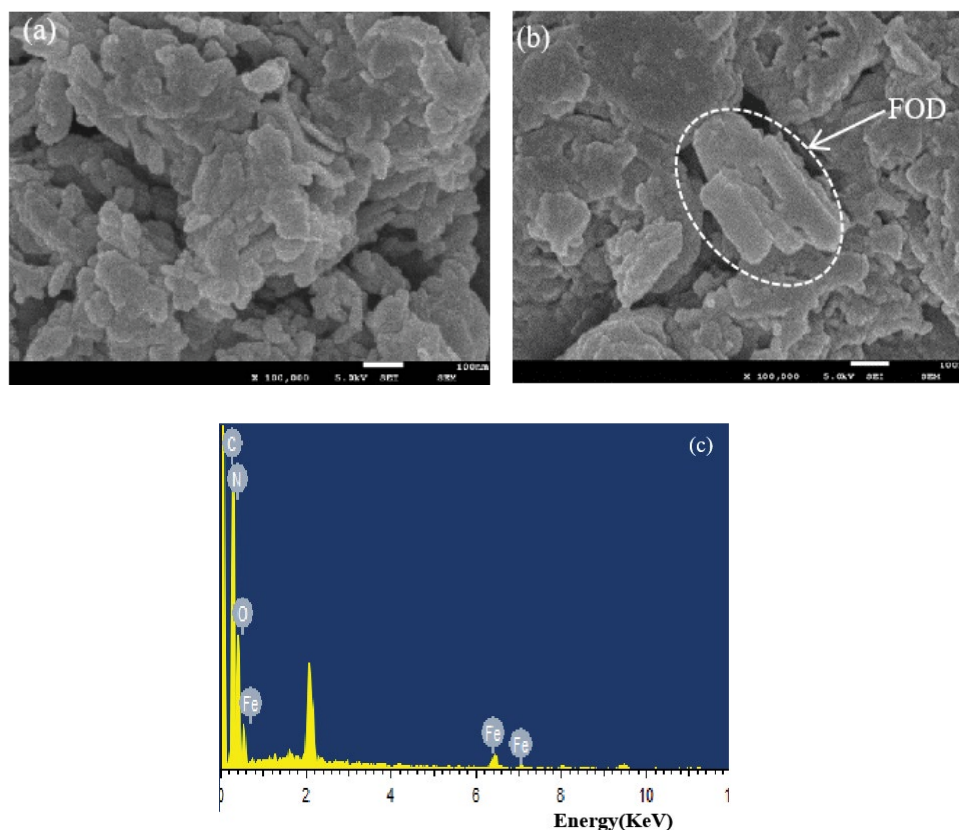


Fig. 1. (a) SEM image of pure CN, (b) SEM image of 10-FOD-CN, and (c) EDX image of 10-FOD-CN.

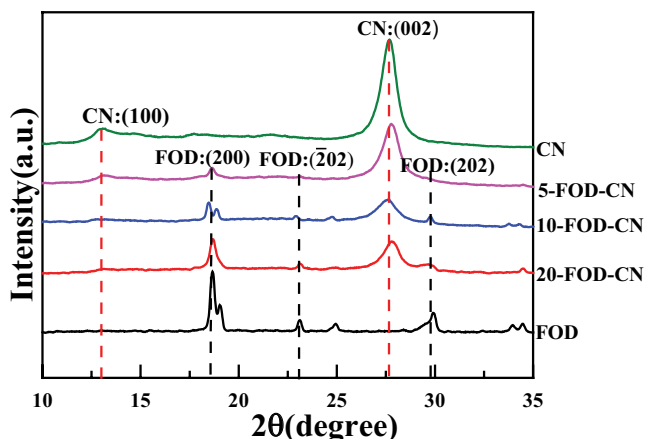


Fig. 2. XRD image of CN and FOD-CN.

The chemical element composition and bond energy of 10-FOD-CN were analyzed via X-ray photoelectron spectroscopy (XPS) (Fig. 4). The elements C, N, O, and Fe can be detected from Fig. 4a in which the XPS image of 10-FOD-CN, was consistent with the results of EDX analysis. The XPS high-resolution images were performed to determine the valence states of C 1s, N 1s, O 1s, and Fe 2p in Figs. 4b–e. The XPS spectra of C 1s had two fitted peaks. The binding energy of 284.6 eV was identified as C–C or C=C,  $sp^2$  hybrid carbon atom, which may be caused by the adsorption of the external carbon to the material's surface or the C–C bond in FOD. The peak of 288.0 eV correspond to N–C=N in CN [30,31] and the O–C=O in FOD [32]. The XPS spectra of N 1s had three peaks, at 398.5, 399.8, and 400.9, respectively. The peak of 398.5 eV corresponded to the C–N=C bond formed by  $sp^2$  hybrid nitrogen atom and carbon, whereas the peaks of 399.8 and 400.9 eV were ascribed to N–(C)<sub>3</sub> and C<sub>2</sub>–N–H, respectively [33]. The spectra of O 1s showed a prominent peak located at 532.0 eV, corresponding to the adsorption of hydroxyl or water on the material's surface [34] or that of the binding water of FOD or C<sub>2</sub>O<sub>4</sub><sup>2-</sup> on FOD [35]. FOD was not the main component of 10-FOD-CN due to the low content. Thus, the peak value in the XPS image of Fe 2p was relatively weak. The peaks of Fe 2p at 709.8 and 723.5 eV were ascribed to the binding energy of Fe<sup>2+</sup> 2p<sub>3/2</sub> and 2p<sub>1/2</sub>, respectively [36,37], suggesting that Fe mainly existed in the form of Fe<sup>2+</sup> when FOD was incorporated with CN.

N<sub>2</sub> adsorption and desorption were performed to obtain the surface area and pore size distribution of the composite catalyst (Fig. 5). The specific surface area was 11.2264 m<sup>2</sup> g<sup>-1</sup>, which was smaller than that of CN (11.5 m<sup>2</sup> g<sup>-1</sup>) synthesized by heat condensation polymerization. Fig. 5b shows that the pore size distribution was approximately 20 nm because the compound FOD affected the specific surface area.

The absorption performance of the catalysts was analyzed using the UV-Vis diffuse reflectance spectrometer (UV-Vis/DRS) (Fig. 6a). The UV-Vis spectrum of pure CN had a wide absorption range of visible light, whereas 10-FOD-CN had no evident red shift, possibly due to the less-doped FOD. The classical Tauc formula  $\alpha h\nu^{1/n} = A(h\nu - E_g)$  [38] was used to calculate the band gap energy ( $E_g$ ). Literature revealed that CN and FOD were direct semiconductors [39]. Thus,

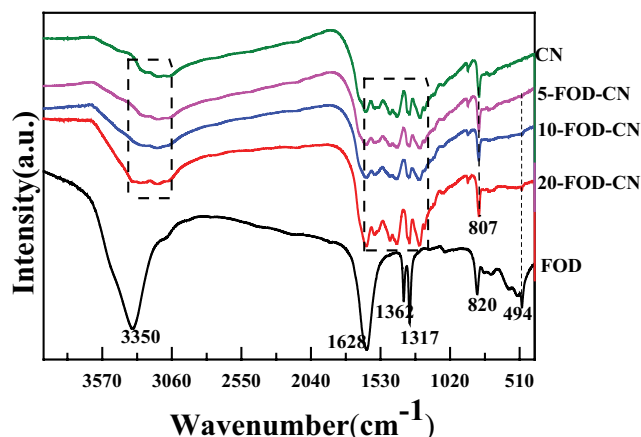


Fig. 3. FT-IR image of CN and FOD-CN.

$n$  was assigned to be  $\frac{1}{2}$ , and then the plot of  $(\alpha h\nu)^2$  vs.  $h\nu$  was obtained in Fig. 6b.  $E_g$  of CN and 10-FOD-CN were derived from the straight part of the extrapolation curve to be approximately 2.80 and 2.75 eV, respectively. Compared with CN, 10-FOD-CN had a slightly enhanced absorption capacity of visible light, indicating that the coupling of CN and FOD could lead to an improvement of visible-light absorption. PL-emission spectra of FOD-CN samples and CN were carried out to verify the effective charge transfer (Fig. 7), which suggests that the composites could enhance the separation of charge carriers.

### 3.2. Photocatalytic experiment

#### 3.2.1. Effect of loading

As shown in Fig. 8a, the FOD-CN composite material had higher degradation efficiency compared with either CN or FOD, which indicating that the combination of CN and FOD was beneficial for the promotion of photocatalytic efficiency. Furthermore, the degradation efficiency for pollutants varied as the FOD content in the composite materials changed. The 10-FOD-CN had better degradation efficiency compared with other composite materials with different proportions and was selected for the following tests. In the absence of oxygen, the degradation effect of 10-FOD-CN was slightly weaker than that in natural conditions under visible-light irradiation, which indicated that the enhancement of reactive oxygen species in the system. Although  $\cdot\text{OH}$  with strong oxidation capacity was mainly produced by FOD, the degradation rate of pollutants by the combined catalyst increased. This result may be due to carriers generated by photoexcited CN, which promoted the photoexcited FOD to generate free radicals ( $\cdot\text{C}_2\text{O}_4^-$  and  $\cdot\text{CO}_2^-$ ) that excite O<sub>2</sub>. The degradation rate decreased with the increase in load, possibly because the load was too high to produce more  $e^-$  and  $h^+$ .

RhB degradation with various catalysts was analyzed to study the reaction kinetics further. The first-order ( $\ln(C_0/C_t) = K_1 t$ ) and the second-order ( $1/C_t - 1/C_0 = K_2 t$ ) kinetic equations were used to fit the degradation. The curves of  $\ln(C_0/C_t)$  vs.  $t$  and  $(1/C_t - 1/C_0)$  vs.  $t$  are plotted in Fig. 9, and the kinetic parameters of the fitted curve are shown in

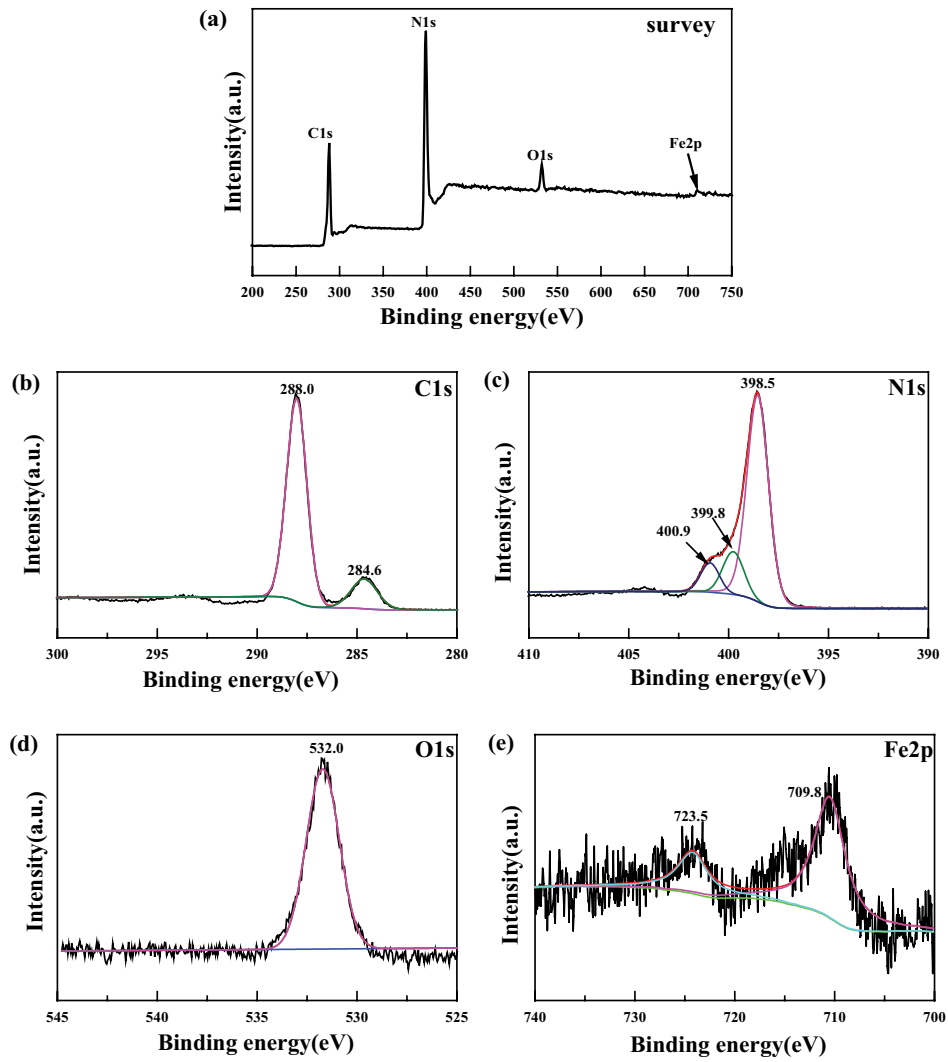


Fig. 4. (a) XPS image of 10-FOD-CN and (b–e) XPS high-resolution images of C 1s, N 1s, O 1s, and Fe 2p, respectively.

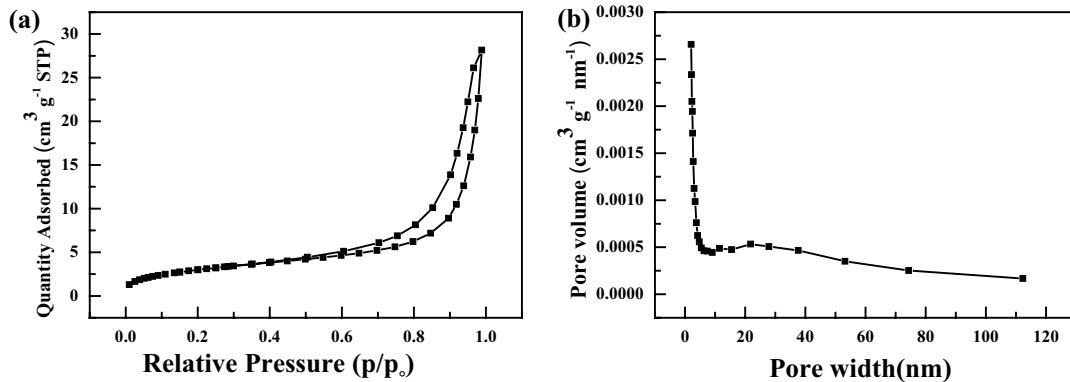


Fig. 5. (a) N<sub>2</sub> adsorption isotherms and (b) pore size distribution of 10-FOD-CN.

Table 1. The photocatalytic degradation of RhB fitted well with the second-order kinetic model. Meanwhile, the reaction rate constant ( $K_2$ ) by using 10-FOD-CN was 6.8, which was 3.4 times higher than that using CN or FOD.

### 3.2.2. Effect of the initial pH

As displayed in Fig. 8b, the pollutant degradation effect was better under acidic conditions because the charge and adsorption capacity of the dye molecules on the surface of

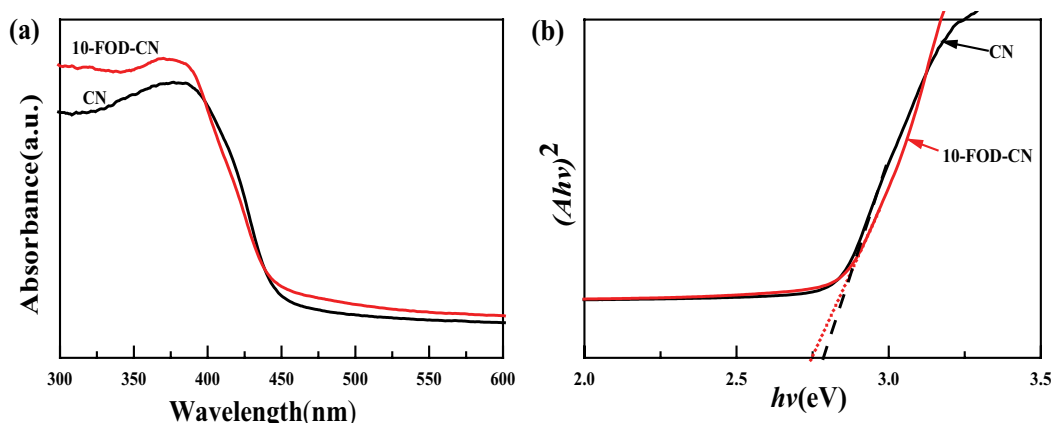


Fig. 6. (a) UV-Vis/DRS of CN and 10-FOD-CN and (b) curves of  $(A\hbar\nu)^2$  and  $\hbar\nu$  of CN and 10-FOD-CN.

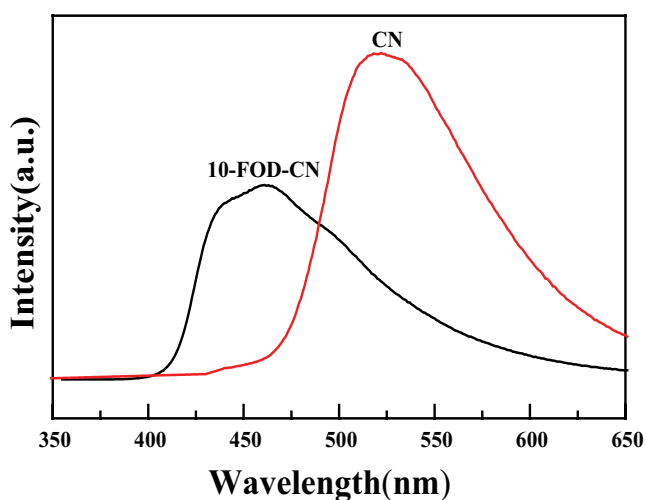


Fig. 7. PL-emission spectra of CN and 10-FOD-CN.

the catalysts were affected by pH [40]. Under acidic conditions, electron transfer was accelerated, and a large amount of  $H^+$  was generated, thereby benefitting the generation of  $\cdot OH$  and significantly enhancing the degradation efficiency. Hence, a pH of 3 was selected for further studies.

### 3.2.3. Effect of the initial concentration of RhB

As shown in Fig. 8c, the degradation rate gradually decreased with the increase in initial concentration in the range of 2–15  $mg L^{-1}$ . When the initial concentration of RhB was high, the pollutant molecules occupied numerous active sites which free radicals were generated. Moreover, the light transmittance of the system weakened, thus affecting the light absorption of the catalyst. As a result, the system had a limited number of active substances and exhibited low degradation rate. At very low initial concentration (2 or 5  $mg L^{-1}$ ), it was difficult to truly evaluate the efficiency of the catalyst. Therefore, 10  $mg L^{-1}$  was selected to evaluate the degradation efficiency of the catalyst.

### 3.2.4. Effect of catalyst dosage

As shown in Fig. 8d, the dosage of the catalyst did not change the degradation rate significantly. When the dosage of the catalyst was 0.1  $g L^{-1}$ , the efficiency was limited due to the diminished active sites. After the dosage exceeded 0.1  $g L^{-1}$ , the degradation efficiency became higher due to the increased number of active sites. At a catalyst dosage of 0.2  $g L^{-1}$ , the degradation efficiency reached 78%. However, as the dosage continued to increase, the degradation efficiency was slightly suppressed possibly because the

Table 1  
Parameters for the kinetic models

Catalyst	Parameters for a first-order kinetic model		Parameters for a second-order kinetic model	
	$K_1 (\times 10^{-3} \text{ min}^{-1})$	$R^2$	$K_2 (\times 10^{-3} \text{ min}^{-1})$	$R^2$
CN	2.12	0.99167	1.24	0.99650
FOD	3.63	0.84834	2.48	0.89171
5-FOD-CN	4.64	0.89722	3.42	0.94444
10-FOD-CN	8.73	0.97118	8.45	0.99845
20-FOD-CN	7.91	0.97757	7.40	0.99974
30-FOD-CN	7.62	0.97820	7.18	0.99963
50-FOD-CN	6.64	0.98318	5.54	0.99946

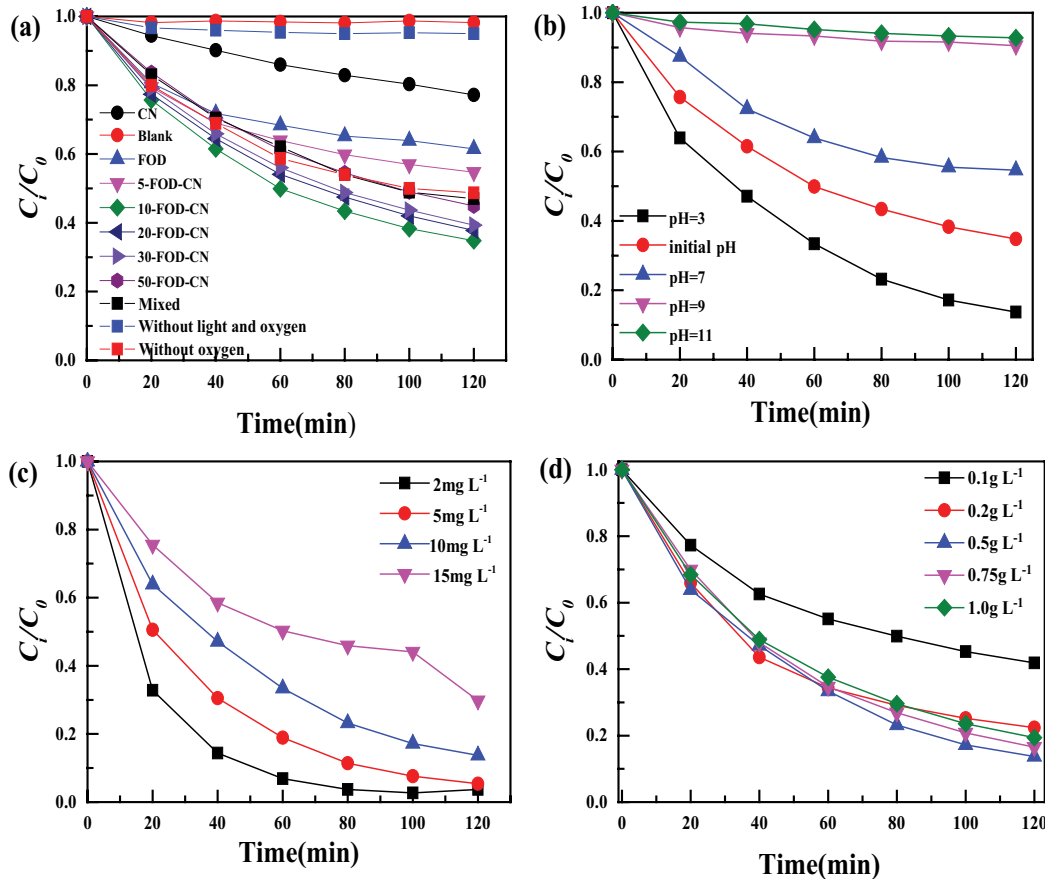


Fig. 8. (a) Effect of loading, (b) effect of pH, (c) effect of the dosage of the catalyst, and (d) effect of the initial concentration of RhB.

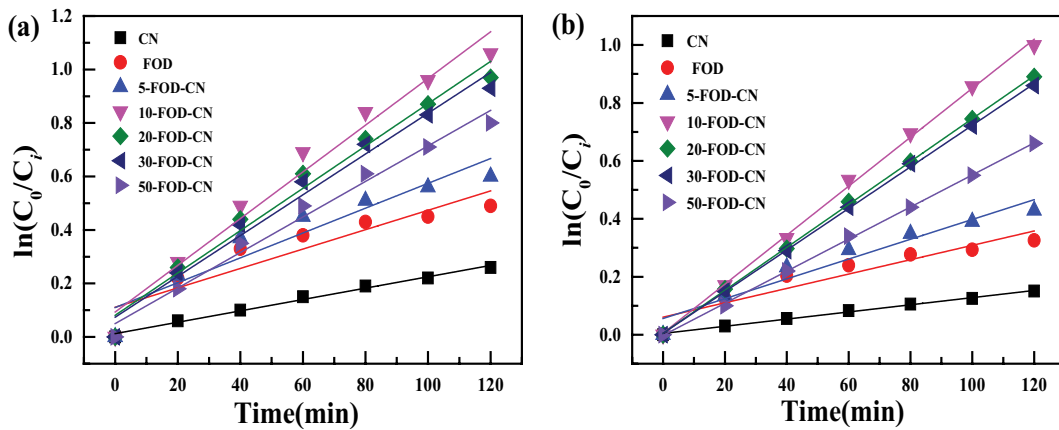


Fig. 9. Fitting of the degradation process of RhB with using various catalysts (a) first-order and (b) second-order kinetic equations.

excessive addition of catalyst resulted in the boosted turbidity of the system. This phenomenon hindered the production of active substances by the catalyst distant from the light source and consequently caused a wastage of the catalyst.

To elucidate the products of the photocatalytic degradation of RhB, Fig. 10 shows the UV-Vis absorption spectra of RhB at different degradation times. As shown in Fig. 10, the absorption peak at approximately 554 nm gradually dropped with the extension of irradiation time, and no other peak

was formed in the process. The trend of the UV-Vis absorption spectra suggested that the pollutants were completely degraded to  $\text{CO}_2$  and  $\text{H}_2\text{O}$  rather than other substances.

### 3.3. Reusability of the catalyst and its possible mechanism

During  $\text{Fe}^{2+}$  activation, oxalate was converted into  $\text{CO}_2$ , resulting in the fading of oxalate and the dissolution of  $\text{Fe}^{2+}$  [19]. Therefore, the reusability of the catalyst in this

process was low (Fig. 11a). When the catalyst was reused, the degradation efficiency was only half that of the first time of usage. A leaching test of Fe was performed to evaluate the stability of the samples. The results are shown in Fig. 11b. Fe accumulation increased with time, because  $\cdot\text{OH}$  destroyed the chain structure formed by iron and oxalate. Through the XRD analysis of the used catalyst (Fig. 11d), the FOD characteristic peaks have disappeared in the used catalyst after 120 min degradation, resulting in the low reusability

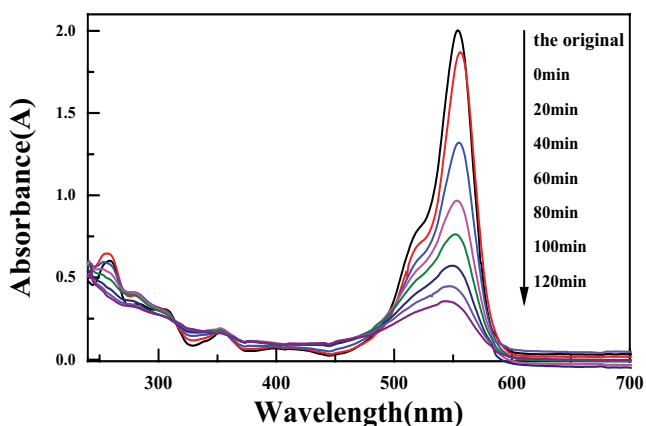


Fig. 10. UV-Vis absorption spectra of RhB in photocatalytic degradation.

and poor stability of the catalyst. The results implied that ferrous oxalate played an important role in the degradation of pollutants.

The dominant free radical ( $\cdot\text{O}_2^-$ ,  $\cdot\text{OH}$ , or  $\text{h}^+$ ) was determined to improve the removal rate; the experimental results of the quenching agent with free radicals (*p*-benzoquinone (BQ), *tert*-butanol (TB), and potash iodide (KI), corresponding to the curves *j*, *k*, and *l*, respectively) in the reaction are shown in Fig. 11c. In the figure, the pollutants were mainly affected by the free radicals of  $\cdot\text{O}_2^-$  and  $\cdot\text{OH}$  within the first 40 min. Curve *k* and *l* had a turning point when the degradation reaction reached 40 min. As shown in curve *k*, the effect of TB on  $\cdot\text{OH}$  was weakened, indicating that the reaction system contained less  $\cdot\text{OH}$  after 40 min. This result was mainly due to the consumption of  $\text{C}_2\text{O}_4^{2-}$ , resulting in a decrease in the amount of  $\cdot\text{OH}$ . Such decrease indicated that  $\cdot\text{OH}$  in the reaction system was mainly produced by  $\text{H}_2\text{O}_2$  generated by carbon-centered free radicals ( $\cdot\text{C}_2\text{O}_4^-$  and  $\cdot\text{CO}_2^-$ ) activating molecular oxygen. In curve *j*, BQ always maintained the inhibition of  $\cdot\text{O}_2^-$ , whether prior to or after 40 min.  $\cdot\text{O}_2^-$  was indirectly converted into  $\cdot\text{OH}$ , which acted on pollutants before 40 min. After 40 min, it was primarily generated by  $\text{e}^-$ , synthesized by the photoexcited CN, to reduce  $\text{O}_2$ . In addition, the degradation rate was twice as much as that of 40–80 min because the first 40 min was mainly composed of  $\cdot\text{OH}$  with strong oxidation capacity. Before 40 min, the contaminant was quickly consumed. Thus, the chromaticity was lowered, and the transmittance

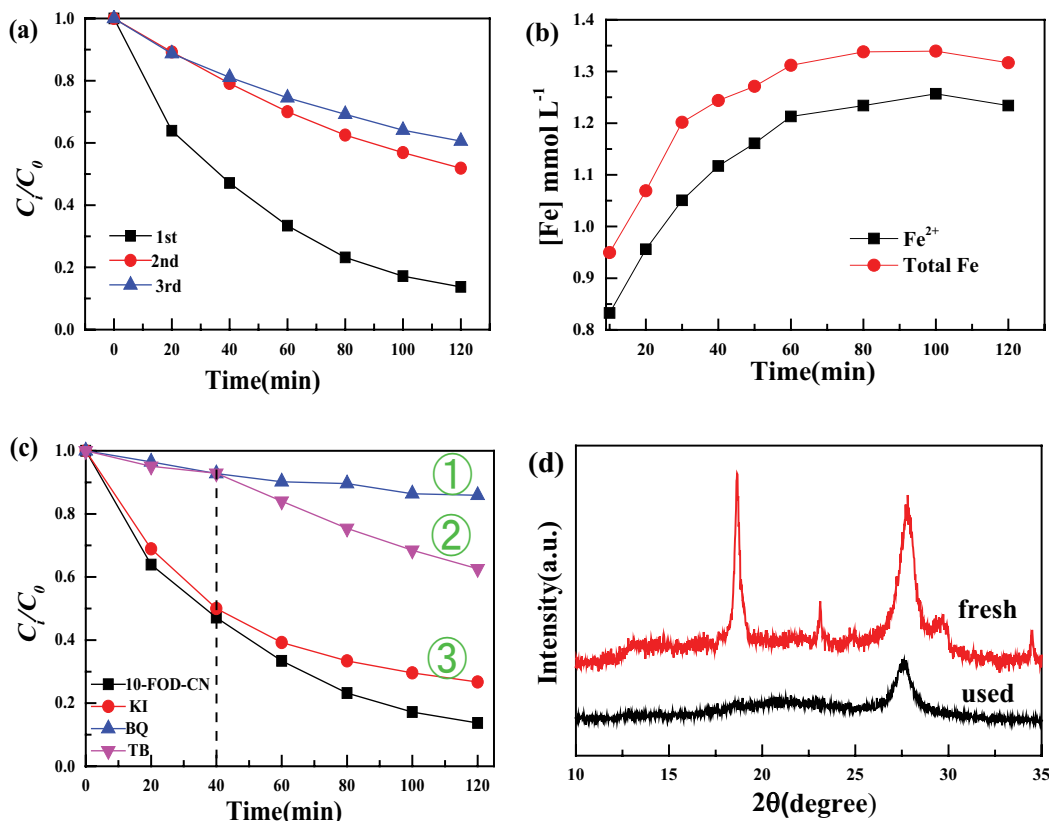
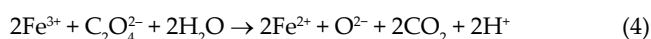


Fig. 11. (a) Recycling curves, (b) Fe accumulation in the reaction system, (c) quenching experiment of free radical, and (d) XRD image of the fresh and used catalysts.

was enhanced. After 40 min, the pollutants were mainly degraded by  $e^-$  (forming  $\cdot O_2^-$ ) combined with  $h^+$ .

In accordance with the results of photocatalytic degradation experiments, the possible degradation pathway was concluded, and the degradation mechanism was proposed (Fig. 12). The reaction system could degrade pollutants by photocatalysis and Fenton-like reaction. In the reaction, semiconductors were excited to generate  $h^+$  and  $e^-$  reducing  $O_2$  to  $\cdot O_2^-$  (Eq. 1). In the system,  $C_2O_4^{2-}$  had two roles: (1) the carbon-centered free radicals ( $\cdot C_2O_4^-$  and  $\cdot CO_2^-$ ) generated the photoexcited FOD in Eqs. (2) and (3). This conclusion has been proven by literature [41,42].  $\cdot C_2O_4^-$  and  $\cdot CO_2^-$  could form  $\cdot O_2^-$  combined with  $H^+$  to synthesize  $H_2O_2$  in Eq. (5) and further decompose into  $\cdot OH$  in Eq. (6). (2)  $C_2O_4^{2-}$  could reduce  $Fe^{3+}$ , thereby promoting the cycle of  $Fe^{3+}$  and  $Fe^{2+}$  in Eq. (4) and improving the utilization rate of  $H_2O_2$  [43]. Moreover,  $C_2O_4^{2-}$  could chelate  $Fe^{3+}$  to form a complex and prevent  $Fe^{3+}$  from precipitating in the reaction, thus effectively facilitating iron circulation.



#### 4. Conclusions

In summary, the catalyst materials of CN-FOD were synthesized through a facile and cost-effective method. The developed catalyst materials exhibited excellent photocatalytic efficiency for RhB under light irradiation without the use of any other auxiliary reagents. The combination of

CN-FOD inhibited the recombination of electrons and holes and greatly improved the utilization rate of the carrier and the photocatalytic efficiency. Thus, the proposed catalyst composite mildly addressed the problems in which the formation of sludge in Fenton reaction caused the secondary pollution and lowered the cycle efficiency of  $Fe^{3+}$  and  $Fe^{2+}$ . Generally speaking, the proposed method reduced cost and resources for the pollutant degradation and avoided the generation of secondary pollution. On the basis of work, innovative ideas for Fenton-like reactions and enhancement strategies for photocatalytic activity are expected using  $g-C_3N_4$ . In the future, the synthetic method of FOD can be optimized to improve the stability and reusability rate of the catalyst.

#### References

- [1] Y. Zhang, M. Sivakumar, S. Yang, K. Enever, M. Ramezani-pour, Application of solar energy in water treatment processes: a review, *Desalination*, 428 (2018) 116–145.
- [2] R. Aguirre Ocampo, F. Echeverria Echeverria, Effect of the anodization parameters on  $TiO_2$  nanotubes characteristics produced in aqueous electrolytes with CMC, *Appl. Surf. Sci.*, 469 (2019) 994–1006.
- [3] N.N. Tusar, D. Maucec, M. Rangus, I. Arcon, M. Mazaj, M. Cotman, A. Pintar, V. Kaucic, Manganese functionalized silicate nanoparticles as a Fenton-type catalyst for water purification by advanced oxidation processes (AOP), *Adv. Funct. Mater.*, 22 (2012) 820–826.
- [4] H. Dong, X. Guo, C. Yang, Z. Ouyang, Synthesis of  $g-C_3N_4$  by different precursors under burning explosion effect and its photocatalytic degradation for tylosin, *Appl. Catal., B*, 230 (2018) 65–76.
- [5] Y. Hong, Y. Jiang, C. Li, W. Fan, X. Yan, M. Yan, W. Shi, In-situ synthesis of direct solid-state Z-scheme  $V_2O_5/g-C_3N_4$  heterojunctions with enhanced visible light efficiency in photocatalytic degradation of pollutants, *Appl. Catal., B*, 180 (2016) 663–673.
- [6] Y.Y. Li, Y. Si, E.X. Han, W.Q. Huang, W.Y. Hu, A.L. Pan, X.X. Fan, G.F. Huang, Steering charge kinetics boost the photocatalytic activity of graphitic carbon nitride: heteroatom-mediated spatial charge separation and transfer, *J. Phys. D-Appl. Phys.*, 53 (2020) 015502.
- [7] W. Guo, J. Zhang, G. Li, C. Xu, Enhanced photocatalytic activity of P-type (K, Fe) co-doped  $g-C_3N_4$  synthesized in self-generated  $NH_3$  atmosphere, *Appl. Surf. Sci.*, 470 (2019) 99–106.
- [8] F. Zeng, W.Q. Huang, J.H. Xiao, Y.Y. Li, W. Peng, W.Y. Hu, K. Li, G.F. Huang, Isotype heterojunction  $g-C_3N_4/g-C_3N_4$  nanosheets as 2D support to highly dispersed 0D metal oxide nanoparticles: generalized self-assembly and its high photocatalytic activity, *J. Phys. D-Appl. Phys.*, 52 (2019) 025501.
- [9] T. Guo, K. Wang, G.K. Zhang, X.Y. Wu, A novel  $\alpha-Fe_2O_3@g-C_3N_4$  catalyst: synthesis derived from Fe-based MOF and its superior photo-Fenton performance, *Appl. Surf. Sci.*, 469 (2019) 331–339.
- [10] K. Wang, J. Li, G. Zhang, Ag-bridged Z-scheme 2D/2D  $Bi_3FeTi_3O_{15}/g-C_3N_4$  heterojunction for enhanced photocatalysis: mediator-induced interfacial charge transfer and mechanism insights, *ACS Appl. Mater. Interfaces*, 11 (2019) 27686–27696.
- [11] Y. Ling, G.Z. Liao, P. Xu, L.S. Li, Fast mineralization of acetaminophen by highly dispersed Ag- $g-C_3N_4$  hybrid assisted photocatalytic ozonation, *Sep. Purif. Technol.*, 216 (2019) 1–8.
- [12] Y.Y. Li, Y. Si, B.X. Zhou, W.Q. Huang, W.Y. Hu, A.L. Pan, X.X. Fan, G.F. Huang, Strategy to boost catalytic activity of polymeric carbon nitride: synergistic effect of controllable in situ surface engineering and morphology, *Nanoscale*, 11 (2019) 16393–16405.
- [13] Z.S. Hang, H.L. Yu, L.P. Luo, X. Huai, Nanoporous  $g-C_3N_4$ /MOF: high-performance photoinitiator for UV-curable coating, *J. Mater. Sci.*, 54 (2019) 13959–13972.

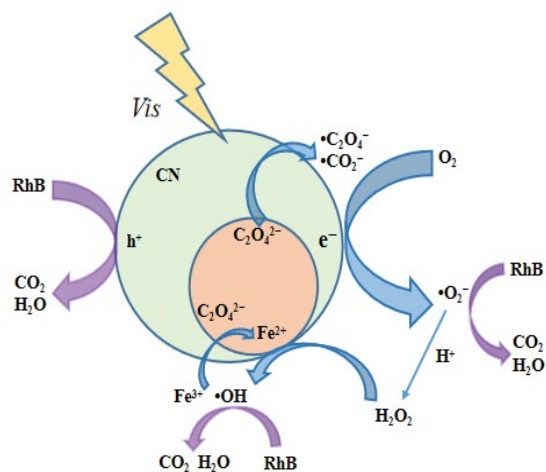


Fig. 12. Degradation mechanism.

- [14] C.C. Wang, X.H. Yi, P. Wang, Powerful combination of MOFs and  $C_3N_4$  for enhanced photocatalytic performance, *Appl. Catal., B*, 247 (2019) 24–48.
- [15] M.D. Allendorf, C.A. Bauer, R.K. Bhakta, R.J.T. Houk, Luminescent metal-organic frameworks, *Chem. Soc. Rev.*, 38 (2009) 1330–1352.
- [16] R. Babarao, J.W. Jiang, Unprecedentedly high selective adsorption of gas mixtures in rho zeolite-like metal-organic framework: a molecular simulation study, *J. Am. Chem. Soc.*, 131 (2009) 11417–11425.
- [17] T. Yamada, M. Sadakiyo, H. Kitagawa, High proton conductivity of one-dimensional ferrous oxalate dihydrate, *J. Am. Chem. Soc.*, 131 (2009) 3144–3145.
- [18] X. Fan, L. Zhang, M. Li, M. Wang, X. Zhou, R. Cheng, Y. Zhou, J. Shi, Alpha-ferrous oxalate dihydrate: a simple coordination polymer featuring photocatalytic and photo-initiated Fenton oxidations, *Sci. China Mater.*, 59 (2016) 574–580.
- [19] L. Hu, P. Wang, S. Xiong, S. Chen, X. Yin, L. Wang, H. Wang, The attractive efficiency contributed by the in-situ reactivation of ferrous oxalate in heterogeneous Fenton process, *Appl. Surf. Sci.*, 467 (2019) 185–192.
- [20] K. Li, Y. Liang, J. Yang, G. Yang, R. Xu, X. Xie, Alpha-ferrous oxalate dihydrate: an Fe-based one-dimensional metal organic framework with extraordinary photocatalytic and Fenton activities, *Catal. Sci. Technol.*, 8 (2018) 6057–6061.
- [21] N. Chen, H. Shang, S. Tao, X. Wang, G. Zhan, H. Li, Z. An, J. Yang, L. Zhang, Visible light driven organic pollutants degradation with hydrothermally carbonized sewage sludge and oxalate via molecular oxygen activation, *Environ. Sci. Technol.*, 52 (2018) 12656–12666.
- [22] A. Angermann, J. Toepfer, Synthesis of magnetite nanoparticles by thermal decomposition of ferrous oxalate dihydrate, *J. Mater. Sci.*, 43 (2008) 5123–5130.
- [23] G. Liao, S. Chen, X. Quan, H. Yu, H. Zhao, Graphene oxide modified  $g-C_3N_4$  hybrid with enhanced photocatalytic capability under visible light irradiation, *J. Mater. Sci.*, 22 (2012) 2721–2726.
- [24] W. Guo, K. Fan, J. Zhang, C. Xu, 2D/2D Z-scheme  $Bi_2WO_6$ /porous- $g-C_3N_4$  with synergy of adsorption and visible-light-driven photodegradation, *Appl. Surf. Sci.*, 447 (2018) 125–134.
- [25] Y. Zhao, Z. Liu, W. Chu, L. Song, Z. Zhang, D. Yu, Y. Tian, S. Xie, L. Sun, Large-scale synthesis of nitrogen-rich carbon nitride microfibers by using graphitic carbon nitride as precursor, *Adv. Mater.*, 20 (2008) 1777–1781.
- [26] L. Liu, Y. Qi, J. Lu, S. Lin, W. An, Y. Liang, W. Cui, A stable  $Ag_3PO_4@g-C_3N_4$  hybrid core@shell composite with enhanced visible light photocatalytic degradation, *Appl. Catal., B*, 183 (2016) 133–141.
- [27] Q. Liu, Y. Guo, Z. Chen, Z. Zhang, X. Fang, Constructing a novel ternary Fe(III)/graphene/ $g-C_3N_4$  composite photocatalyst with enhanced visible-light driven photocatalytic activity via interfacial charge transfer effect, *Appl. Catal., B*, 183 (2016) 231–241.
- [28] M.A. Gabal, Non-isothermal decomposition of  $NiC_2O_4-FeC_2O_4$  mixture aiming at the production of  $NiFe_2O_4$ , *J. Phys. Chem. Solids*, 64 (2003) 1375–1385.
- [29] D. Li, S.J. Li, Y. Zhang, J.J. Jiang, W.J. Gong, J.H. Wang, Z.D. Zhang, Monodisperse water-soluble gamma- $Fe_2O_3$ /polyvinylpyrrolidone nanoparticles for a magnetic resonance imaging contrast agent, *J. Phys. Chem. Solids*, 19 (2015) S358–S362.
- [30] Y. Liao, S. Zhu, J. Ma, Z. Sun, C. Yin, C. Zhu, X. Lou, D. Zhang, Tailoring the morphology of  $g-C_3N_4$  by self-assembly towards high photocatalytic performance, *ChemCatChem*, 6 (2014) 3419–3425.
- [31] J. Di, J. Xia, S. Yin, H. Xu, L. Xu, Y. Xu, M. He, H. Li, Preparation of sphere-like  $g-C_3N_4$ /BiOI photocatalysts via a reactable ionic liquid for visible-light-driven photocatalytic degradation of pollutants, *J. Mater. Chem. A*, 2 (2014) 5340–5351.
- [32] Y. Yang, X. Fan, G. Casillas, Z. Peng, G. Ruan, G. Wang, M.J. Yacaman, J.M. Tour, Three-dimensional nanoporous  $Fe_3O_4/Fe_3C$ -graphene heterogeneous thin films for lithium-ion batteries, *ACS Nano*, 8 (2014) 3939–3946.
- [33] Q. Xu, C. Jiang, B. Cheng, J. Yu, Enhanced visible-light photocatalytic  $H_2$ -generation activity of carbon/ $g-C_3N_4$  nanocomposites prepared by two-step thermal treatment, *Dalton Trans.*, 46 (2017) 10611–10619.
- [34] J. Zou, J. Gao, Y. Wang, Synthesis of highly active  $H_2O_2$ -sensitized sulfated titania nanoparticles with a response to visible light, *J. Photochem. Photobiol., A*, 202 (2009) 28–135.
- [35] S.H. Yoo, D. Jang, H.I. Joh, S. Lee, Iron oxide/porous carbon as a heterogeneous Fenton catalyst for fast decomposition of hydrogen peroxide and efficient removal of methylene blue, *J. Mater. Chem. A*, 5 (2017) 748–755.
- [36] D. Wilson, M.A. Langell, XPS analysis of oleylamine/oleic acid capped  $Fe_3O_4$  nanoparticles as a function of temperature, *Appl. Surf. Sci.*, 303 (2014) 6–13.
- [37] H.A. Bicalho, J.L. Lopez, I. Binatti, P.F.R. Batista, J.D. Ardisson, R.R. Resende, E. Lorencon, Facile synthesis of highly dispersed Fe(II)-doped  $g-C_3N_4$  and its application in Fenton-like catalysis, *Mol. Catal.*, 435 (2017) 156–165.
- [38] L. Jiang, X. Yuan, G. Zeng, J. Liang, Z. Wu, H. Yu, D. Mo, H. Wang, Z. Xiao, C. Zhou, Nitrogen self-doped  $g-C_3N_4$  nanosheets with tunable band structures for enhanced photocatalytic tetracycline degradation, *J. Colloid Interface Sci.*, 536 (2019) 17–29.
- [39] M.C. Li, W.X. Wang, M.Y. Yang, F.C. Lv, L.J. Cao, Y.G. Tang, R. Sun, Z.G. Lu, Large-scale fabrication of porous carbon-decorated iron oxide microcuboids from Fe-MOF as high-performance anode materials for lithium-ion batteries, *RSC Adv.*, 5 (2015) 7356–7362.
- [40] H. Zhang, L.H. Guo, L. Zhao, B. Wan, Y. Yang, Switching oxygen reduction pathway by exfoliating graphitic carbon nitride for enhanced photocatalytic phenol degradation, *J. Phys. Chem. Lett.*, 6 (2015) 958–963.
- [41] M. Vedrenne, R. Vasquez-Medrano, D. Prato-Garcia, B.A. Frontana-Uribe, M. Hernandez-Esparza, J. Manuel de Andres, A ferrous oxalate mediated photo-Fenton system: toward an increased biodegradability of indigo dyed wastewaters, *J. Hazard. Mater.*, 243 (2012) 292–301.
- [42] J. Li, C. Xiao, K. Wang, Y. Li, G.K. Zhang, Enhanced generation of reactive oxygen species under visible light irradiation by adjusting the exposed facet of  $FeWO_4$  nanosheets to activate oxalic acid for organic pollutant removal and Cr(VI) reduction, *Environ. Sci. Technol.*, 539 (2019) 11023–11030.
- [43] J.M. Monteagudo, A. Duran, I. San Martin, M. Aguirre, Effect of continuous addition of  $H_2O_2$  and air injection on ferrioxalate-assisted solar photo-Fenton degradation of Orange II, *Appl. Catal., B*, 89 (2009) 510–518.